Appl Phys B (2010) 101: 773–789
DOI 10.1007/s00340-010-4327-9

Applied Physics B
Lasers and Optics

Characterization and optimization of the laser-produced plasma EUV source at 13.5 nm based on a double-stream Xe/He gas puff target

R. Rakowski · A. Bartnik · H. Fiedorowicz · F. de Gaufridy de Dortan · R. Jarocki · J. Kostecki · J. Mikołajczyk · L. Ryć · M. Szczurek · P. Wachulak

Received: 23 February 2010 / Revised version: 2 November 2010 / Published online: 23 November 2010

Abstract The paper describes a debris-free, efficient laser-produced plasma source emitting EUV radiation. The source is based on a double-stream Xe/He gas-puff. Its properties and spectroscopic signatures are characterized and discussed. The spatio-spectral features of the EUV emission are investigated. We show a large body of results related to the intensity and brightness of the EUV emission, its spatial, temporal, and angular behavior and the effect of the repetition rate as well. A conversion efficiency of laser energy into EUV in-band energy at 13.5 nm of 0.42% has been gained. The electron temperature and electron density of the source were estimated by means of a novel method using the FLY code. The experimental data and the Hullac code calculations are compared and discussed. The source is well suited for EUV metrology purposes. The potential of the source for application in EUV lithography was earlier demonstrated in the optical characterization of Mo/Si multi-layer mirrors and photo-etching of polymers.

R. Rakowski (✉) · A. Bartnik · H. Fiedorowicz · R. Jarocki · J. Kostecki · J. Mikołajczyk · M. Szczurek · P. Wachulak
Institute of Optoelectronics, Military University of Technology, 2 Gen. Sylwestra Kaliskiego St., 00-908 Warsaw, Poland
e-mail: rafal.rakowski@post.pl
Fax: +48-22-6668950

Present address:
R. Rakowski
Department of Physics, Lund University, Lund, Sweden

F. de Gaufridy de Dortan
Service des Photons, Atomes et Molecules, CEA-Saclay, 91191 Gif-sur-Yvette Cedex, France

L. Ryć
Institute of Plasma Physics and Laser Microfusion, 23 Hery St., 01-497 Warsaw, Poland

P. Wachulak
Department of Electrical and Computer Engineering, Colorado State University, 1320 Campus Delivery, Fort Collins, CO 80523-1320, USA

1 Introduction

EUV lithography is currently both technically and economically challenging [1]. The miniaturization in electronics strongly depends on the EUV technology progress acquiring powerful EUV light sources [2]. Recently, a growing number of compact EUV plasma sources have been developed including laser-produced plasmas (LPP) [3, 4]. The EUV source for exposure tools for high-volume manufacturing basically has to meet industrial requirements of power in-band (at 13.5 nm within 2% BW) and may not have an impact on the lifetime of the reflective optics. This power limitation leads to the demand on the EUV power into the half sphere of 400 W/2π in the laser-produced plasmas (LPP) case and of 1 kW/2π for gas discharge-produced plasmas (GDPP) [4]. To our knowledge, the highest EUV power (measured on intermediate focus (IF) point) of 104 W (115 W required) reached until now using the CO_2 laser with the pre-pulse was recently reported [5].

Besides an application of the EUV source in exposure tools in EUV lithography, it is also of interest to inspect fabricated electronic circuits as well as components of the EUV projection tools: multi-layer interference coatings, masks or resists [2]. EUV metrology growth should keep up with the development of other EUV technologies. To address these problems, debris-free sources and droplet mitigation systems are under construction for EUV metrology purposes

Fig. 1 Experimental setup

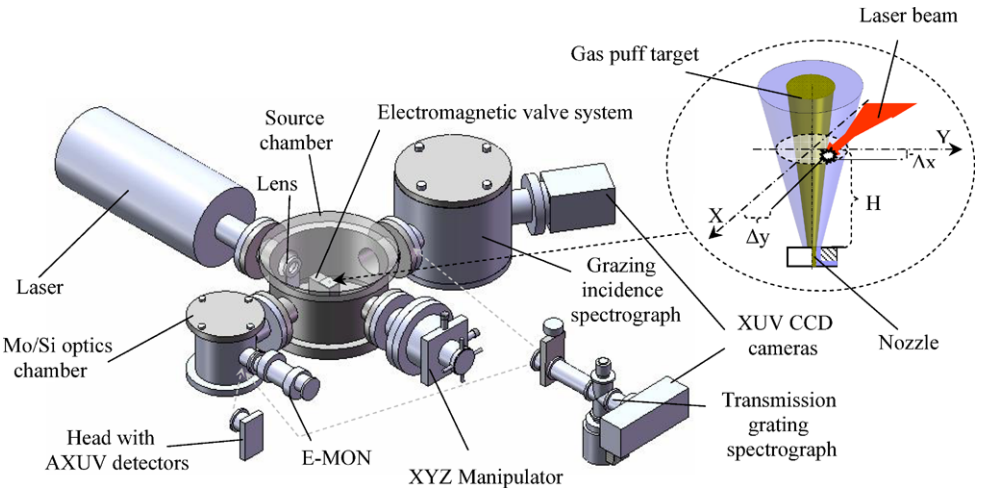

[5–13]. Nevertheless, much work remains to be done in this field. It was demonstrated that a LPP source utilizing noble gas, for instance xenon, is a debris-free, to some extent point-like EUV and soft X-ray source [14, 15].

In this paper, we demonstrate and characterize a laser-produced plasma EUV source based on a double-stream Xe/He gas-puff target that belongs to the group of mass-limited targets [16]. The concept of using this target for the short wavelength radiation generation was proposed in 1992 at the Institute of Optoelectronics (IOE), Warsaw [17]. The double-stream gas-puff target is formed by the injection of gas under high pressure through the nozzles of an electromagnetic valve system driven synchronously by the laser power supply. The valve system is described elsewhere [15]. Xenon is the driver gas which flows through a cylindrical orifice into a hollow stream of an outer gas-helium injected by an annular orifice in a concentric manner with the cylindrical one [18]. The EUV emission attained from the gas-puff target is comparable to the emission from solid state targets [19]. It was found by using a Faraday cup detector that the source based on the gas puff target is debris-free (no ions, droplets, etc.) with a vacuum better than 10^{-6} mbar (M. Suzuki, private communication, 2002). It is due to the shielding effect of the buffering helium stream that efficiently suppresses the amount of debris. The source can be applied as a compact EUV lamp for EUV metrology purposes. An application of the source for the optical characterization of Mo/Si multi-layer mirrors [20–26] was previously reported [27]. Besides the EUV metrology, the laser-produced plasma source with the Xe/He gas-puff target has been successfully used in photo-etching of polymers [28, 29].

Alternatively to the laser produced-plasma EUV source presented in this paper, X-ray tubes were considered for EUV metrology purposes, despite the fact that there are three orders of magnitude lower intensities as compared to the described source [30]. An EUV metrology program at the Bessy II synchrotron facility in Berlin was also initiated [31].

2 Experimental conditions

Our investigations on the EUV emission were performed using two distinctly different configurations of the experimental arrangement. In the first configuration, a 25 mm focal length lens (Edmund Optics prod.) focuses the laser pulse onto the xenon jet to generate the EUV plasma source. In the second configuration, the lens (CVI prod.) has the focal length of 50 mm. A schematic diagram of the latter experimental setup with the EUV lamp is presented in Fig. 1. The EUV lamp was developed based on optimization measurements of the former setup.

In both configurations, the setup was equipped with the same compact Nd:YAG laser (energy per pulse $E = 0.55$ J, pulse duration $t = 3.9$ ns (FWHM), $M^2 = 2.5$, repetition rate f_{rep} up to 10 Hz). In the EUV lamp case, the laser was installed inside a metal tube to avoid accidental laser beam exposure. Two different lenses were used to compare the influence of various laser beam distributions and the laser irradiance on EUV emission. Another reason was to investigate the interactions between EUV radiation and the glass optics for different plasma-to-lens distances. When using the $f = 25$ mm lens, the laser spot was approximately 100 μm in diameter giving the power density of 1.8×10^{12} W/cm^2. Such a relatively big spot size has been preliminary predicted to ensure proper plasma conditions for optimal emission in the EUV region. Tighter focusing results in a higher electron temperature, thus shifting the peak of plasma emission toward XUV radiation. When using the $f = 50$ mm lens, a spot size of 70 μm could be obtained that led to the power density of 3.6×10^{12} W/cm^2. Higher power

density at a longer focal length lens was achieved due to lower lens aberrations. The setup in both configurations consisted of three main components: the laser, an experimental chamber with an electromagnetic valve system to produce the gas puff target, and measurement equipment to characterize EUV emission. The measurement equipment (described elsewhere [32–34]) consisted of a free-standing transmission grating (Heidenhain GmbH prod.) and a flat field grazing incidence grating (Hitachi prod.) spectrographs equipped with a CCD camera, a pinhole camera, calibrated EUV monitors, and semiconductor photodiodes (IRD prod.). The transmission grating was created in a pinhole of 50 μm in diameter [34]. The arrangement allowed for broad investigations of the laser-plasma EUV source such as imaging of the source and obtaining spectral, temporal, and angular distributions of radiation. The wavelength calibration of the spectra has been done based on recorded and identified lithium-like lines from the oxygen plasma. The grazing incidence spectrograph (GIS) spectra were determined with an accuracy of 0.5 Å in comparison with the theoretically calculated lines by Churilov et al. [35]. The spectral resolution of the GIS was about 0.2 Å in the EUV range and that of the transmission grating spectrograph (TGS) was about 0.6 nm. The measurements of the in-band intensity of EUV pulses were performed in the single-shot mode and the repetition mode as well using a calibrated E-MON energy meter (Jenoptik prod.).

3 Spectral investigations

3.1 Measurements with the grazing incidence spectrograph

One of the key issues in the EUV source development is an optimization of in-band emission. Using the GIS, the dependence of EUV emission on the time delay between the moments of time when the valves are opened and the laser pulse arrives as well as on the laser focal spot position in regard to the gas puff target was investigated. The spectral measurements for both lenses of $f = 25$ mm and 50 mm focal length were performed. At the beginning of our research, it was assumed that the gas density in the target should be the highest attainable to assure a high conversion efficiency (CE) of the laser energy into EUV radiation. To tune the gas density, the time delays for the xenon gas and the outer gas were varied. It was found experimentally that, due to an opacity effect produced by surrounding neutral and low-ionized Xe ions, the maximum gas density measured for the delay $\Delta t_{\mathrm{Xe,H\ or\ He}} = 800$ μs was not optimal for the most efficient generation of EUV radiation [15]. It was found that for the delay $\Delta t_{\mathrm{Xe}} = 800$ μs, the optimum time delay for the auxiliary gas (either H or He) was $\Delta t_{\mathrm{H,He}} = 350$ μs [32]. The spectra for the $f = 25$ mm lens corresponding to the optimum cases of $\Delta t_{\mathrm{H,He}}$ are presented in Fig. 2. The EUV yield at ~13.5 nm wavelength is greater in the case of the Xe/H target; nevertheless, the observed UTA (Unidentified Transition Array [36]) peaks at around 11 nm are comparable. The UTA mainly consists of emissions from Xe^{10+} to Xe $^{13+}$ ions [37, 38]. The double peak UTA structure observed for the Xe/H target (red solid line) occurs for optimum parameters only when the Xe^{10+} ion has the largest population [37]. The peak at the shorter wavelength corresponds to the strong emission due to the Xe^{13+} 4d–4f transition and that at the longer wavelength is related to the significant emission due to the Xe^{10+} 4d–4f transition. For the Xe/H target, the Xe^{10+} ion is also the predominantly radiating ion at 13.5 nm (4d–5p transition), leading evidently to higher intensities in this region as compared to the Xe/He target (dashed blue line).

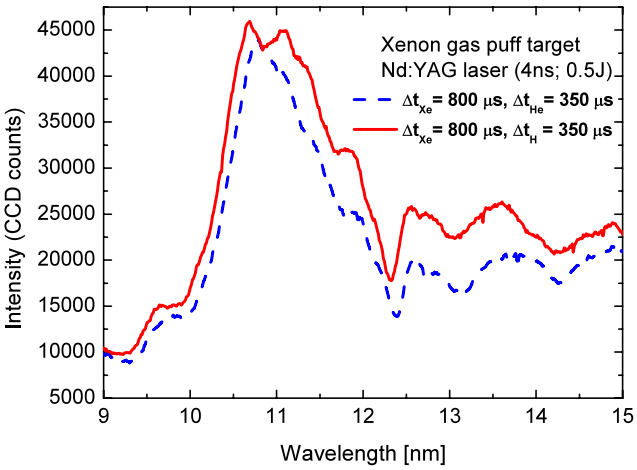

Fig. 2 Spectral distributions of Xe/He and Xe/H targets at optimum time delay

Hydrogen, helium, or argon as buffering outer gases were employed in order to investigate the influence of the opacity of the surrounding neutral and low-ionized Xe ions on the EUV in-band emission. The relative intensities at 13.5 nm wavelength were estimated from the spectra obtained in the single-shot mode (see Fig. 3). In the high repetition rate regime, argon was taken as the outer gas, because it is heavier than H or He resulting in a much easier evacuation of this gas out of the chamber. It was questionable whether the greater absorption of argon (if compared to He or H) could be compensated by its faster evacuation. The results indicate the highest EUV emission for the Xe/H target. However, lightweight hydrogen requires a long evacuation time several times that of He to reach the initial vacuum level after each laser shot. Argon and hydrogen as outer gases were finally not further considered: Argon due to a too low an in-band intensity and hydrogen due to a too long an evacuation time in single-shot operation.

The influence of the backing pressure and the focusing condition (spatial position of the laser beam in the gas puff

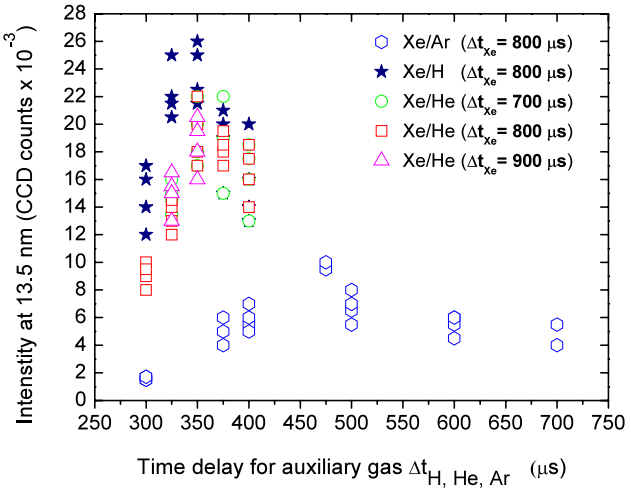

Fig. 3 Emission at 13.5 nm for Xe/He, Xe/H, and Xe/Ar targets for various time delays of the buffering gas

target) on the EUV emission was investigated using the 50 mm focal length lens. The spectra obtained parameters optimal for significant EUV in-band emission are depicted in Figs. 4a–4b.

Comparing the spectra obtained for both lenses, one can notice that the ratio of the feature at 13.5 nm and the UTA peak at ~10.8 nm for the $f = 50$ mm lens is approximately one-third (after subtraction of the continuum background, cf. Fig. 4a) whereas it is one half for the case of the $f = 25$ mm lens (cf. Fig. 2). The peak of the UTA centered at 10.8 nm is unaltered in all cases but the width (FWHM) of the UTA structure differs slightly in each case, which is typical for mass-limited targets [37]. In Fig. 4a, the absorption resonance lines are marked indicating that plasma in this spectral range is optically thick and emission is suppressed by absorption [39, 40]. In Fig. 4b, the focal spot lies at the interface between Xe and He ($\Delta y = 900$ μm and backing pressures $P_{\mathrm{Xe,He}} = 1$ MPa). The greatest intensity measured with a calibrated photodiode corresponded to $\Delta y = 900$ μm as well, but occurred for $P_{\mathrm{Xe}} = 1.5$ MPa and $P_{\mathrm{He}} = 0.2$ MPa. In Fig. 4b, three dominant clearly distinguishable features ($4d^8\ ^3F_3$–$4d^7(^2G)5p\ ^3F_3$, $4d^8\ ^3F_3$–$4d^7(^2H)5p\ ^3G_4$, $4d^8\ ^1G_4$–$4d^7(^2G)5p\ ^1G_4$) of the in-band Xe^{+10}4d-5p transition are presented [41]. Recently, it has been calculated that the emission around 13.5 nm is supported not only by transitions in Xe^{+10} as it has been previously assumed, but also by transitions in Xe^{+9}, considering satellite lines and interaction of configurations [42]. Actually, those calculated spectra agree fairly well with the experimental ones presented in this work.

3.2 Measurements with the transmission grating spectrograph

In order to extend the spectral investigation of the EUV source, the TGS was utilized which allows realizing absolute

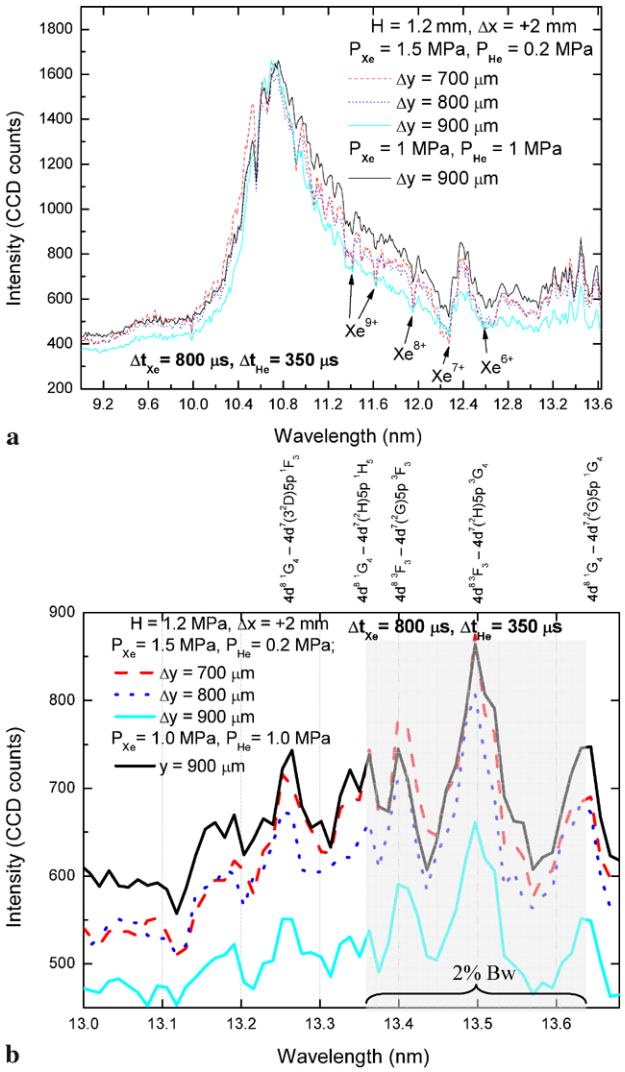

Fig. 4 Spectra obtained for Xe/He plasma: (**a**) for optimum conditions in the EUV range, (**b**) same but enlarged for the in-band range

measurements and characterize the spatial distribution of radiation emission regions vs. wavelength. By means of the TGS setup, the influence of the laser spot position (focusing condition) and the time delay on the in-band EUV intensity, for $f = 25$ mm lens was investigated. Owing to the circular shape of the gas puff target cross-section in the laser beam and y-axis plane (see Fig. 1), the plasma dimensions in the range of 0.2–1.6 mm for different Δy positions were obtained. This also influenced the spectra. Due to the inhomogeneous distribution of the gas density and the electron temperature for selected regions in the plasma, varying spectral distributions were observed. In Fig. 5a, a typical spectral image for arbitrarily selected focusing conditions ($H = 1$ mm, $\Delta x = +1$ mm, $\Delta y = +0.1$ mm) is presented; in Fig. 5b, the corresponding spectral distributions in the EUV range for various cross-sections through the plasma are depicted. In the region 3 to 21 nm, the spectrum consists of two bands

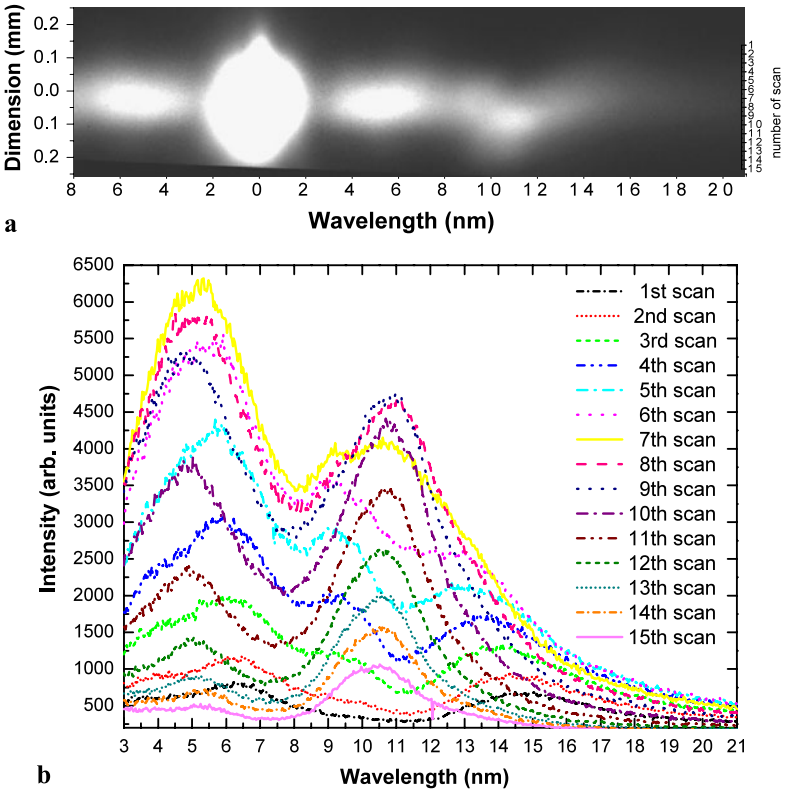

Fig. 5 Typical spectral image from TGS (**a**), and the spectral distributions corresponding with them (**b**), for various cross-sections through the Xe/He plasma for: $H = 1$ mm, $\Delta x = +1$ mm and $\Delta y = +0.1$ mm

centered at 5 and 11 nm, respectively. In Fig. 5a, the central plasma (the middle of the 0th order), due to its high electron temperature, contributes most to the short wavelengths (the peak around 5 nm). The plasma region most suitable for high emission near 11 nm is outside the plasma center. Based on Fig. 5a, the spatial distance between those two regions was determined to be 40 μm.

In Figs. 6a–6b, the spectral distributions for the distances $H = 1$ and 1.5 mm from the laser spot to the orifice exit as a function of the Δy parameter are shown. The detailed explanation of the dominating features in the EUV around 5 and 11 nm is described elsewhere [32]. Here, we show that the influence of the laser focus spot position, Δy, with respect to the gas puff target on the emission efficiency at 13.5 nm is weak at $H = 1$ mm (marked in Fig. 6a with a circle). Support for this comes from the radiogram shown in Fig. 7: wherein the gas stream begins to expand in the direction perpendicular to the gas flow axis for distances only larger than 1 mm from the nozzle exit, where the dimensions of the plasma correspond to the dimensions of the gas puff target. Thus, for $H = 1$ mm, an opacity effect caused by the surrounding gas curtain was absent due to the lack of neutral or low-ionized gas in the plasma vicinity. A merit of that focusing geometry is the possibility to apply it combined with an EUV optical system with a big collecting power, where the radiation can be collected on either side of the plasma. Fig. 6c shows the spectral distributions for different Δx and Fig. 6d for selected H, respectively, keeping other spatial parameters of the laser focus spot position constant. The highest intensity recorded for the 11 nm feature at $\Delta x = +1$ mm was generated by the irradiance in the interaction region of the order of 1.2×10^{11} W/cm^2. $H = 1$ mm was found optimal for efficient emission at 13.5 nm wavelength (depicted in Fig. 6d). Smaller distances (e.g., $H = 0.8$ mm) turned out to be less effective because the xenon density is too high for the limited flux of the input pulse [43]. Fig. 6a reveals that the choice $\Delta x = 0$, $H = 1$ mm is also not optimal since the plasma formed by tight focusing resulted in too high a plasma temperature. Moreover, overdense plasma with critical conditions for the laser wavelength was created in this case [32].

Apart from controlling the plasma dimension, the change of the plasma spatial position was also studied by varying the laser spot position, Δy. The reason of this effect derives from the Δy-dependence of the spatial distribution of the gas density in the target. The pictures presented in Fig. 8a show how the plasma position shifts for $\Delta y = 0$, -0.2, and -0.4 mm at $H = 1$ mm and $\Delta x = +1$ mm. Figure 8b shows the second plasma plume additionally formed in laser direction. Perhaps the shock wave moves the part of the gas target along the laser beam direction, which interacts later with laser radiation transmitted through the plasma.

Due to the relatively low spectral resolution of the TGS (about $\Delta\lambda \approx 0.6$ nm at 13.5 nm), an estimation of the

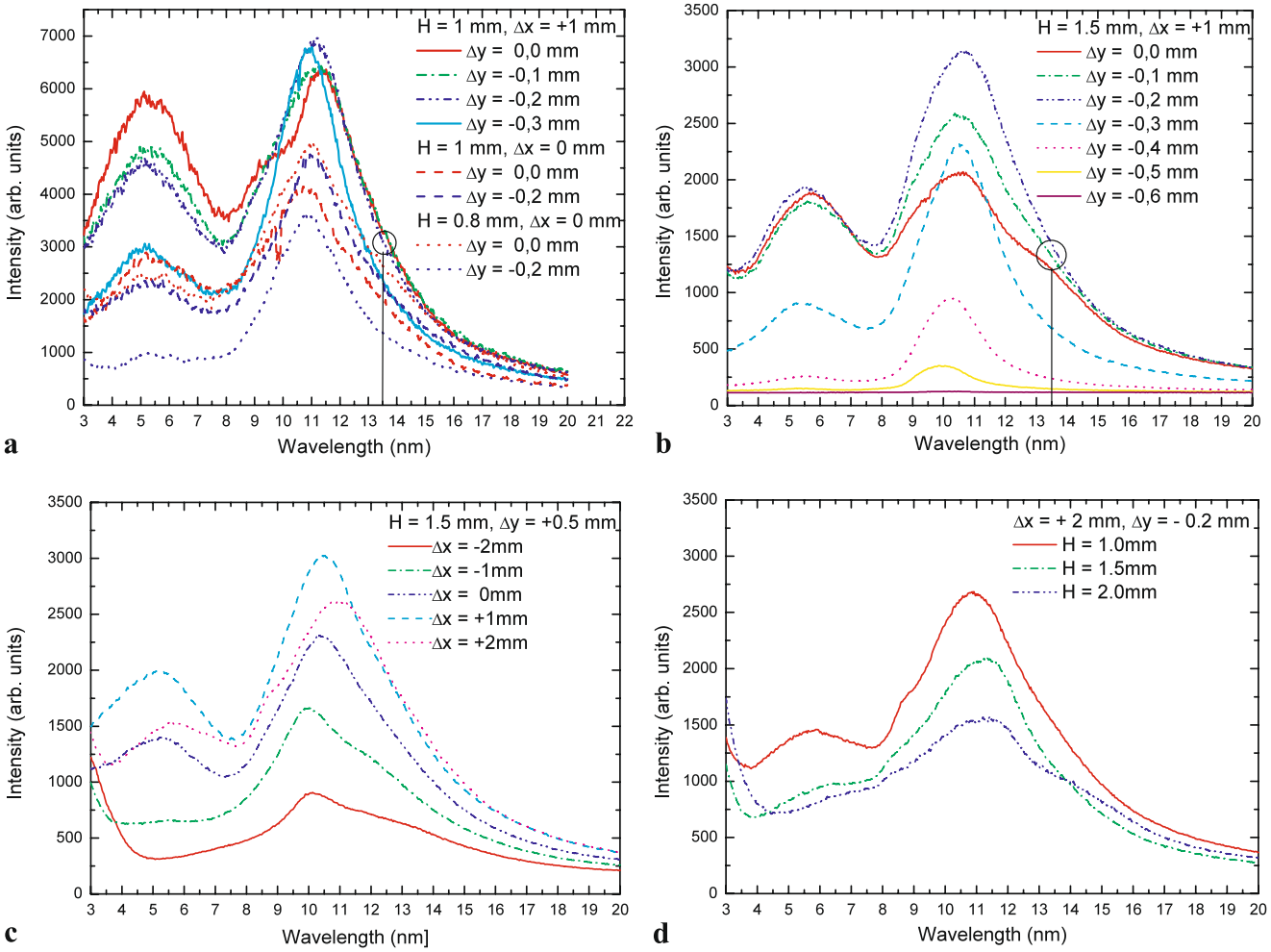

Fig. 6 Spectral distributions obtained from Xe/He plasma for various laser spot positions in relation to the gas puff target. (**a**) $H = 0.8$ mm, $\Delta x = 0$ mm; $H = 1$ mm, $\Delta x = 0$ mm; $H = 1$ mm, $\Delta x = +1$ mm for various Δy. (**b**) $H = 1.5$ mm, $\Delta x = +1$ mm for various Δy. (**c**) $H = 1$ mm, $\Delta y = +0.5$ mm for various Δx. (**d**) $\Delta x = +2$ mm, $\Delta y = -0.2$ mm for various H

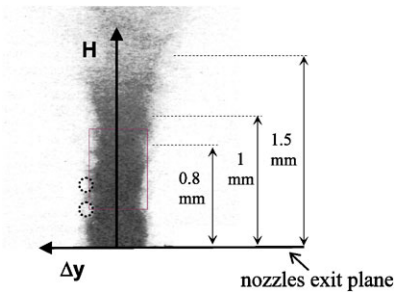

Fig. 7 Typical radiogram of the gas puff target

absolute intensity taken directly from the spectral images was impossible. The use of both the Mo/Si selective mirror (Fraunhofer Institute, Jena, Germany) and the TGS enabled, however, an absolute calculation of the EUV intensity at 13.5 ± 0.5 nm (7.4% of BW). Radiation from the plasma reflected from the Mo/Si wavelength selector was dispersed by the grating. The results obtained for optimum time delays $\Delta t_{Xe} = 800$ µs and $\Delta t_{He} = 350$ µs are shown in Figs. 9a–9c.

The maximum intensity of 1.07 mJ/sr per pulse for $H = 1$ mm, $\Delta x = 0$ µm, $\Delta y = 600$ µm was measured. The highest intensities for $H = 1.5$ mm were about 30% smaller in comparison with the $H = 1$ mm case. Since the TGS was set on the opposite side of the gas puff target in relation to the Mo/Si mirror, the maximum energy yield was measured at a larger distance Δy than the one observed from the spectra (cf. Figs. 6a–6b). The explanation of that can be found in Fig. 7, where retrorse gas stream (on the right) is seen (depicted with the red rectangle) affecting the maximum emission at a 13.5 nm wavelength for different Δy for both the left and right-hand sides of the gas puff target (where the diagnostic tools were positioned). At the edge of the gas column the Kelvin–Helmholtz (perhaps also Rayleigh–Taylor) instabilities are seen, marked with the dashed circles [44, 45].

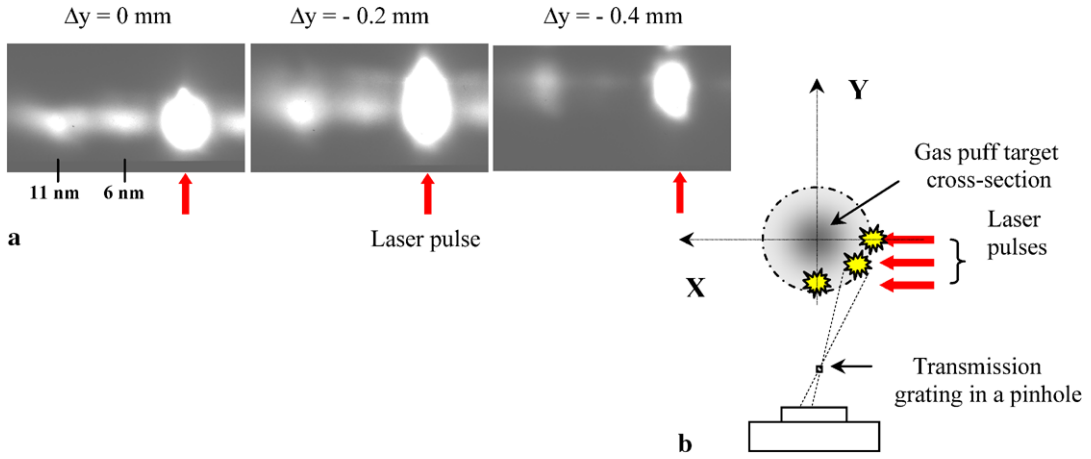

Fig. 8 Plasma position and plasma size change in dependence on Δy. (**a**) Spectra for selected values of Δy, (**b**) scheme of target irradiation

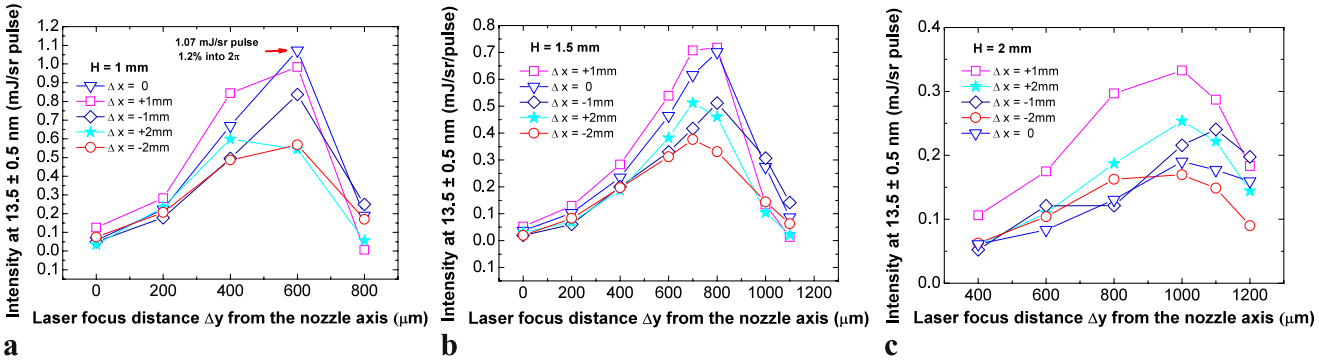

Fig. 9 EUV yield at 13.5 nm (7.4% BW) vs. Δy position for various Δx positions and $H = 1$ mm (**a**), $H = 1.5$ mm (**b**), and $H = 2$ mm (**c**)

The corresponding spectral images and distributions for the case of the 50 mm lens and tight focusing ($\Delta x = 0$ mm) using the TGS are presented in Figs. 10a–10b. Ionization of the Xe diffused into the helium region is seen on the spectral images. Compared to Fig. 10a, more laser energy is transferred to the xenon region in Fig. 10b. It is also evident that significant emission in the EUV region is below 10 nm. The spectral line present around 1.25 nm derives from a Xe ion stage as high as Xe XXXII [46, 47]. The radiation at 13.5 nm wavelength is very weak. The only parameter in which the two spectra differ is Δt_{He}. Fig. 10b indicates the highest T_e observed in our experiments on EUV generation. The spectra are wavelength-calibrated with the use of published Xe^{+10} peaks [35].

4 Spatial investigations of the source

The spectrograph alone is not enough to fully characterize the EUV source. Additional measurements with a pinhole camera revealed shapes, dimensions, and brightness of the plasma source for selected working conditions and parameters. In Fig. 11, selected pinhole plasma images are presented for the $f = 25$ mm lens case and various values of H, Δx, and Δy.

The images were taken using the Mo/Si mirror and an yttrium filter allowing spatial distribution measurements of plasma radiation at 13.5 nm wavelength. In Fig. 11a, small plasma shining at 13.5 nm is observed for tight focusing of the laser beam on the axis of the gas puff target (where both the gas density and the opacity are the highest). The brightest recorded plasma (shown in Fig. 11b) has projection dimensions in the measuring direction of 0.4×0.8 mm^2. At H-distances larger than 1 mm, plasmas were more elongated and less bright (cf. Figs. 11c–11d).

Figure 12 presents the pinhole plasma images for optimal EUV generation and the $f = 50$ mm lens. The plasma dimensions for radiation at 13.5 nm are 1.5 times larger than those for the $f = 25$ mm lens. In Fig. 13, the second plasma seen in the direction of the gas flow is probably due to opacity-induced radiation transport.

From the pinhole camera images, the peak brightness was calculated assuming an area corresponding to the spatial resolution of the pinhole camera. The results for different focusing conditions of the $f = 25$ mm lens are presented in Fig. 14, and those of the $f = 50$ mm lens in

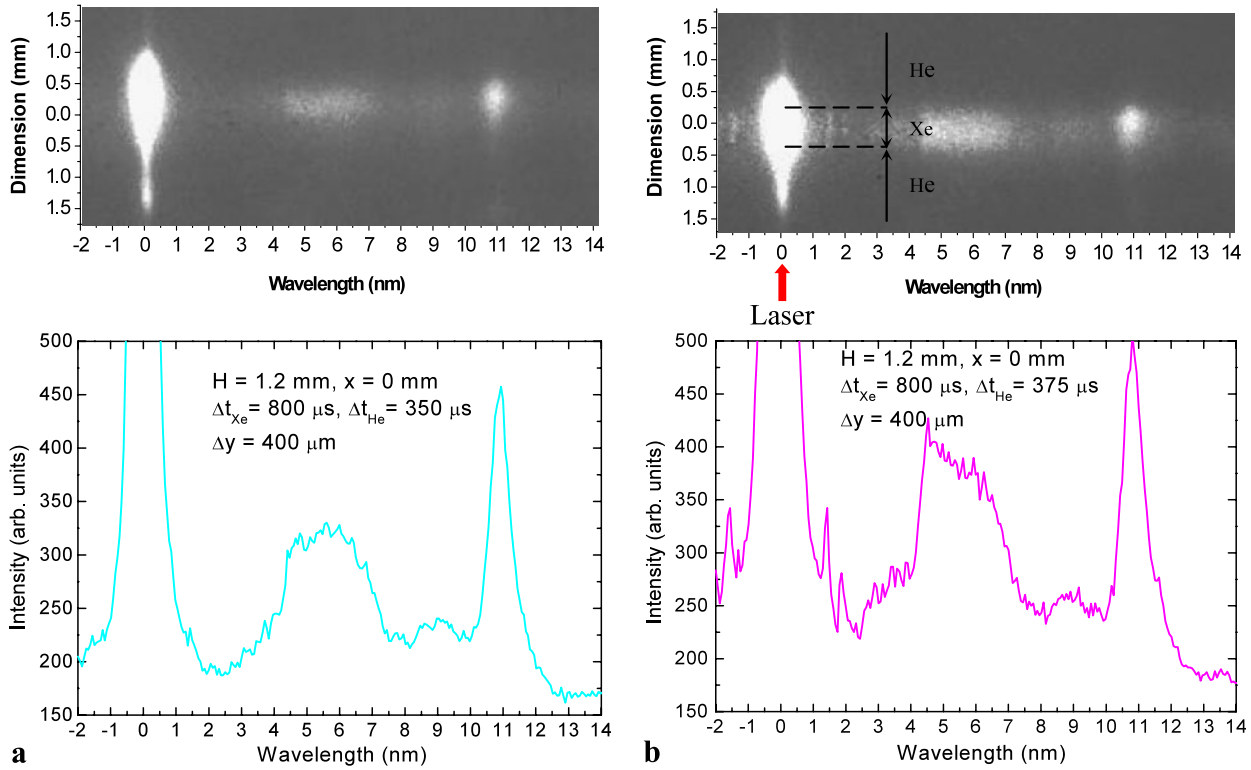

Fig. 10 Spectra and corresponding spectral distributions at tight focusing ($\Delta x = 0$ mm) for the case of the 50 mm lens. (**a**) $\Delta t_{\mathrm{He}} = 350$ μs, (**b**) $\Delta t_{\mathrm{He}} = 375$ μs

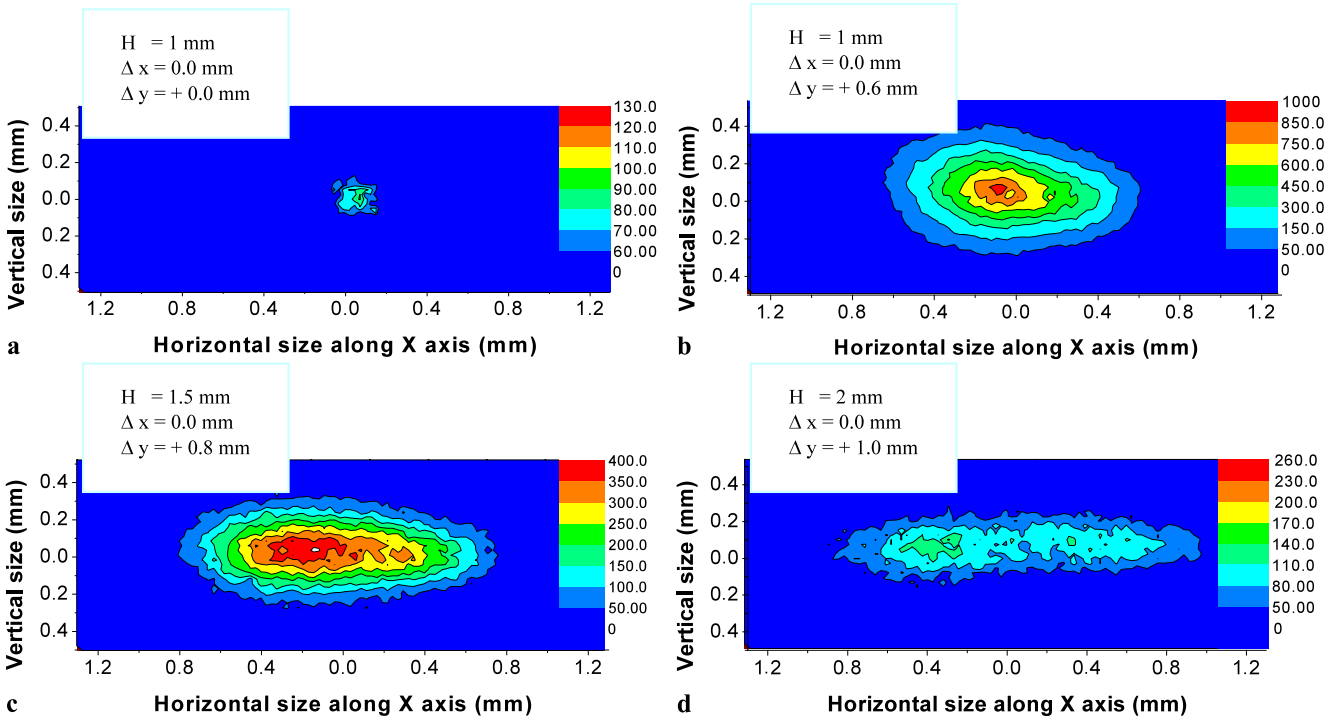

Fig. 11 Pinhole images obtained for 13.5 nm radiation at $H = 1$ mm, 1.5 mm, and 2 mm, $\Delta x = 0$ mm and selected values of Δy. (**a**) 0 mm, (**b**) +0.6 mm, (**c**) +0.8 mm, and (**d**) = +1 mm

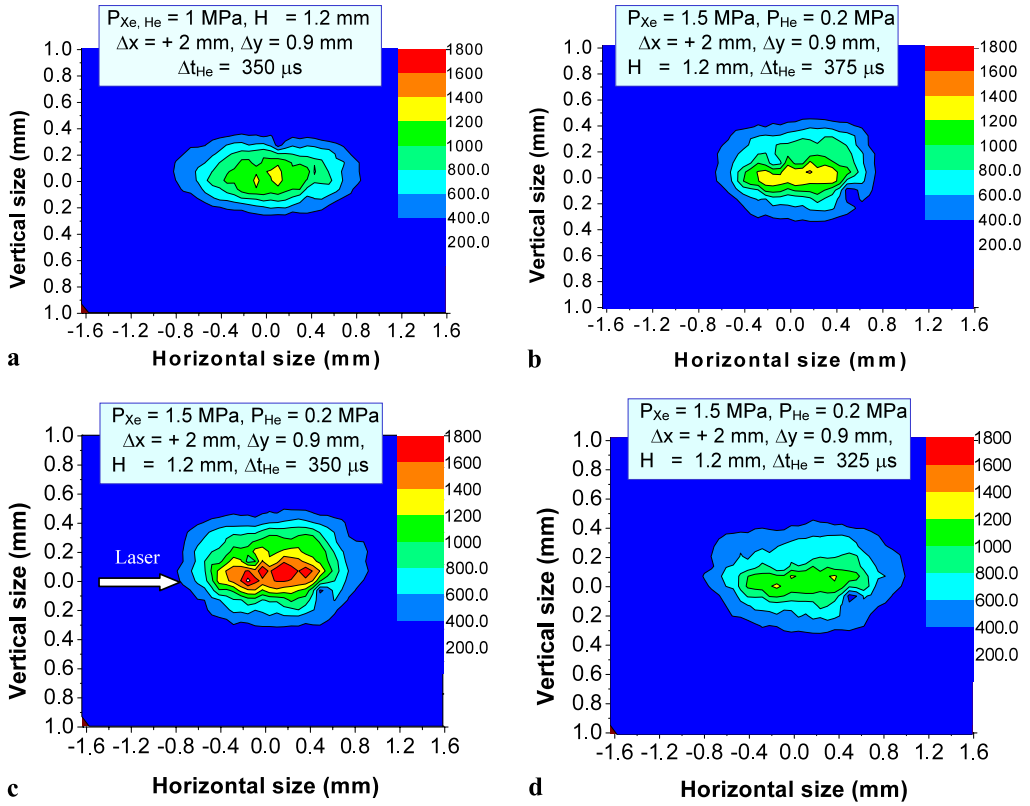

Fig. 12 Pinhole images at 13.5 nm radiation for $H = 1.2$ mm, $\Delta x = +2$ mm, $\Delta y = 0.9$ mm and selected values of Δt_{He}: (**a**) 350 μs at $P_{Xe,He} = 1$ MPa, and optimum backing pressures $P_{Xe} = 1.5$ MPa, $P_{He} = 0.2$ MPa; (**b**) 375 μs, (**c**) 350 μs, and (**d**) 325 μs

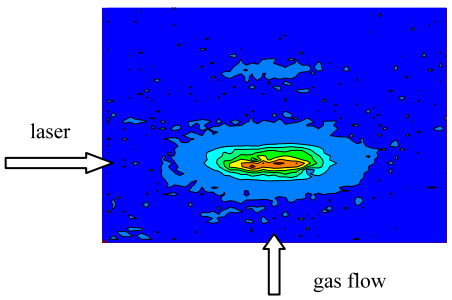

Fig. 13 Pinhole image of the split plasma emission at 13.5 nm

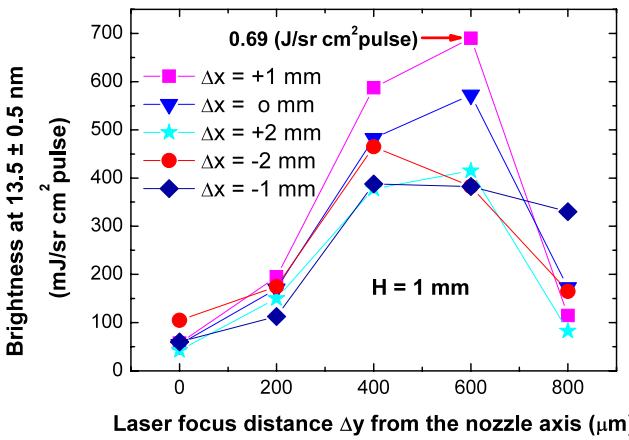

Fig. 14 Brightness for the $f = 25$ mm lens at 13.5 ± 0.5 nm at $H = 1$ mm, Δx in the range (0 mm, ±1 mm, ±2 mm) vs. selected values of Δy

Fig. 15. In the case of the $f = 25$ mm lens, the brightness was investigated for different focusing positions of the laser spot ($H = 1$ mm, $\Delta x = 0$, ±1 mm, ±2 mm) as a function of Δy. There is a coincidence between the optimum parameters ($H = 1$ mm, $\Delta x = +1$ mm, $\Delta y = 600$ μm) for which both intensity and brightness are maximal (compare Figs. 10a and 14). For the $f = 50$ mm lens, the optimum working parameters are $\Delta t_{Xe} = 800$ ms, $\Delta x = +2$ mm, $\Delta y = 0.9$ mm, $H = 1.2$ mm, $P_{Xe} = 1.5$ MPa, and $P_{He} = 0.2$ MPa.

The maximum values of the peak brightness for the $f = 25$ mm lens are much higher than those for the $f = 50$ mm lens. This originates from different conditions as to the interaction of the laser pulse with the gas puff target. In optimal peak brightness cases ($\Delta x = 1$ mm for the $f = 25$ mm lens and $\Delta x = 2$ mm for the $f = 50$ mm lens), the transverse sizes of the laser beam are comparable, thus also laser power densities. However, the gas pressure is higher in the $f = 25$ mm lens case resulting in a smaller and brighter plasma efficiently emitting at 13.5 nm.

5 Absolute EUV measurements

The absolute measurements of the EUV source were performed using calibrated semiconductor detectors and the selective Mo/Si mirror.

5.1 Measurements with the AXUV-100Si/Zr photodiode

For the $f = 25$ mm focusing lens, the emission at 13.5 ± 0.5 nm was investigated as a function of Δy for different Δx positions (0, ± 1 mm, ± 2 mm) and three H distances (1, 1.5, and 2 mm). The results of these measurements are shown in Figs. 16–18. The highest intensities are recorded for the Δy position where the laser spot is at the interface between the Xe and He streams. The cases (a) and (b) correspond to the measurements from the right and left-hand sides of the x-axis, respectively (see Fig. 1). At $H = 1$ mm, the maximum intensity values are similar to each other for the measurements on both sides, but for different Δy ($\Delta y = 200$ µm or $\Delta y = 400$ µm depending on the measuring side). This indicates, as mentioned above, an asymmetry in the formation of the gas puff target (see Fig. 7). When the laser spot is located at $H = 1$ mm, the position of the target is shifted by about 200 µm from the nozzles axis; for $H = 2$ mm this shift is about 400 µm.

The results of EUV intensity measurements using the TGS are in good agreement with the results obtained using photodiodes (compare Fig. 9 and Figs. 16–18).

For the setup configuration using the $f = 50$ mm lens, the influence of the spatial parameters of the laser spot position (Δx, Δy, H) on the EUV emission at 13.5 nm was also investigated. The single-shot EUV intensity values versus Δy are presented in Fig. 19 for selected values of Δx.

Placing the laser spot at the center of the gas puff target ($\Delta x = \Delta y = 0$) was found to be an inefficient way of enlarging in-band emission due to the opacity effect. The best position found is $\Delta x = +2$ mm. However, it is sensitive to small deviations. For $\Delta x = +2.5$ mm and $\Delta x = -3$ mm the laser intensity was below the xenon ionization threshold. Figure 20 shows the emission dependence on Δy for a few H distances. The distance $H = 1.2$ mm yielding the highest emission is the minimum safe distance in the setup. For shorter distances, the nozzle orifice can be damaged by the hot plasma. The influence of backing pressures on the EUV generation for the optimum working conditions (the spatial parameters and the time delay) is presented in Fig. 21.

Evidently, the pressures resulting in the maximum yield at 13.5 nm were $P_{Xe} = 1.5$ MPa and $P_{He} = 0.2$ MPa. The EUV intensity per pulse obtained at these pressures were almost twice as high than that obtained at $P_{Xe} = P_{He} = 1$ MPa. The EUV emission weakly depends on the helium backing pressure for P_{Xe} fixed at 1 MPa. The signals were integrated over the entire surface of the plasma in contrary to the measurements done with the spectrographs equipped

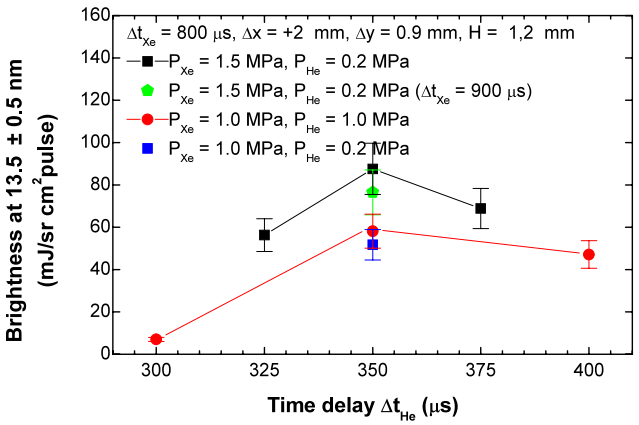

Fig. 15 Brightness for the $f = 50$ mm lens at 13.5 ± 0.5 nm at $H = 1$ mm, Δx in the range (0 mm, ± 1 mm, ± 2 mm) vs. selected Δt_{He}

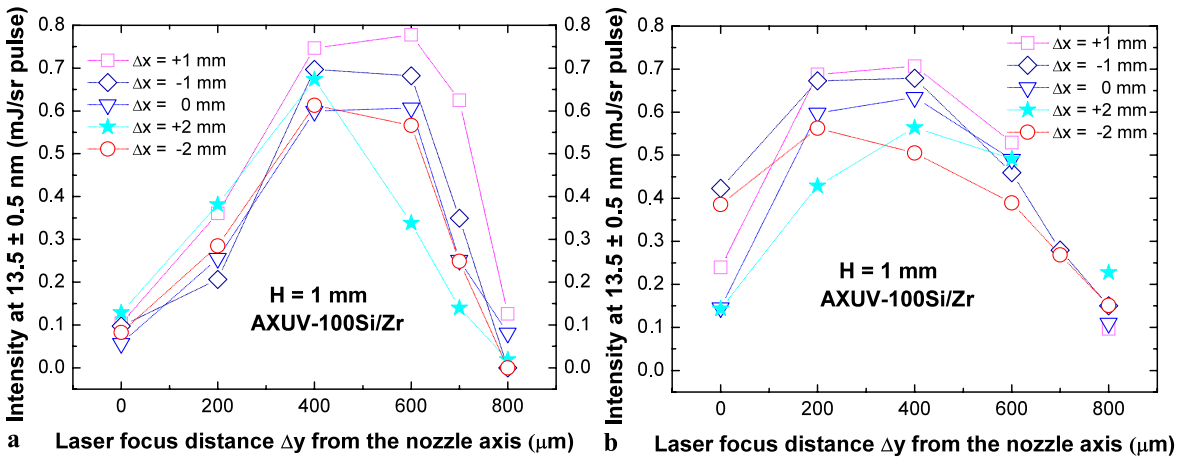

Fig. 16 EUV emission at 13.5 nm for various laser spot positions in relation to the position of the gas puff target at $H = 1$ mm, (**a**) measurements perpendicular to the laser beam on one side of the source chamber, (**b**) measurements on the opposite side

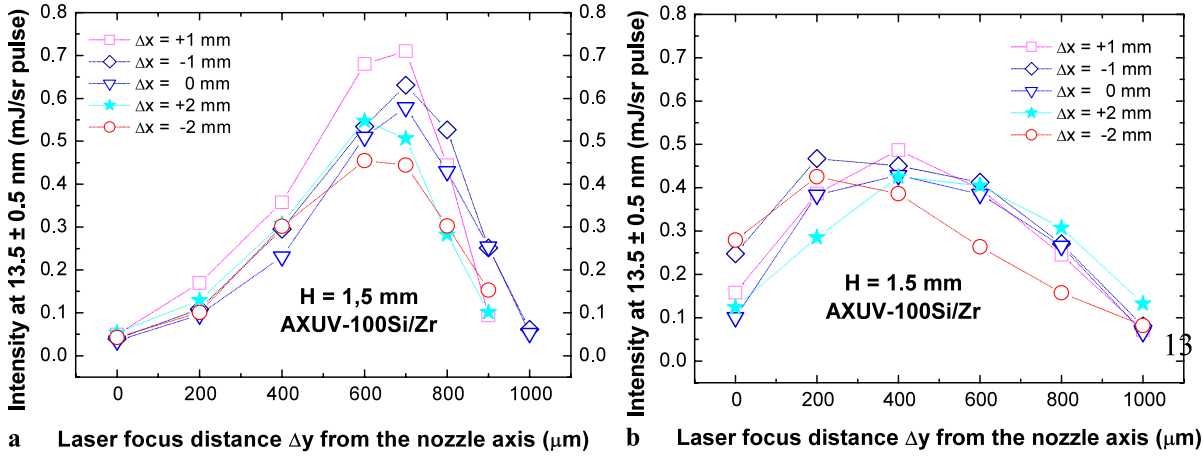

Fig. 17 EUV emission at 13.5 nm for various laser spot positions in relation to the position of the gas puff target at $H = 1.5$ mm, (**a**) measurements perpendicular to the laser beam on one side of the source chamber, (**b**) measurements on the opposite side

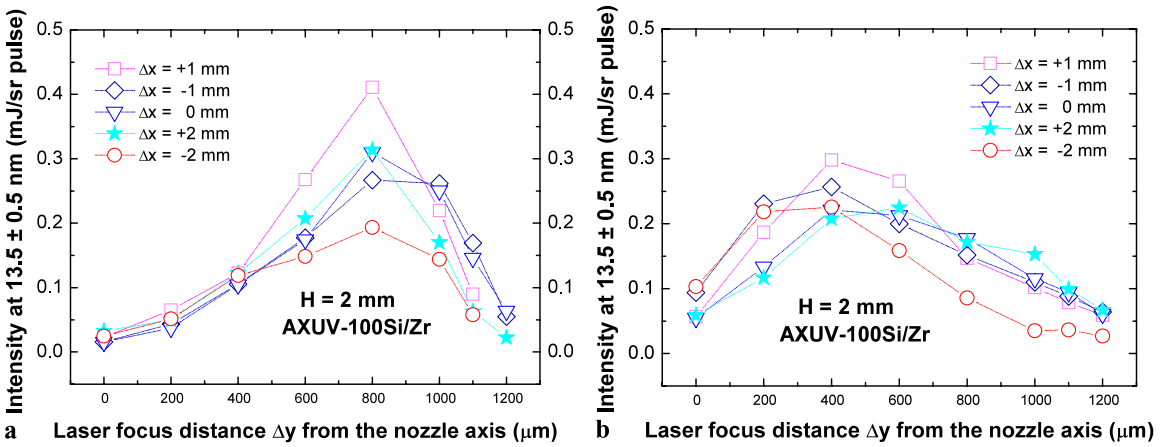

Fig. 18 EUV emission at 13.5 nm for various laser spot positions in relation to the gas puff target at $H = 2$ mm, (**a**) measurements perpendicular to the laser beam on one side of the source chamber, (**b**) measurements on the opposite side

with a slit. Therefore, the optimum backing pressures for highest EUV emission give larger dimensions of the created plasma in comparison with those corresponding to the optimum backing pressures found in the spectrograph measurements, which was also revealed by the pinhole camera measurements.

Additionally, for the $f = 50$ mm lens, the influence of the time delay for helium on the EUV yield in-band was investigated. It has been found that the optimum time delay was $\Delta t_{\mathrm{He}} = 350$ μs, as presented in Fig. 22.

When using the $f = 50$ mm lens, the absolute EUV energy per pulse at 13.5 nm and 7.4% bandwidth is about 10 mJ/2π, corresponding to a conversion efficiency of 2%. For the $f = 25$ mm lens the maximum intensity of the EUV source is about 8 mJ/2π [15]. In order to estimate the in-band conversion efficiency at 2% BW, the calibrated EUV energy meter E-MON was employed, indicating a value of 0.42% for the $f = 50$ mm lens.

5.2 Temporal measurements with the AXUV-HS1 photodiode

The results of EUV intensity measurements using the fast AXUV-HS1 diode for $f = 50$ mm lens are shown in Fig. 23.

The highest EUV in-band emission is recorded for the delays $\Delta t_{\mathrm{He}} = 375$ μs and $\Delta t_{\mathrm{He}} = 350$ μs, for which the error bars overlap. The pulse duration of the EUV signal was between 3.7 and 3.8 ns for optimum conditions, while the pumping pulse duration was equal to 3.9 ns. A low signal-to-noise ratio resulted in a high error of the pulse duration measurements for Δt_{He} other than 350 μs and 375 μs.

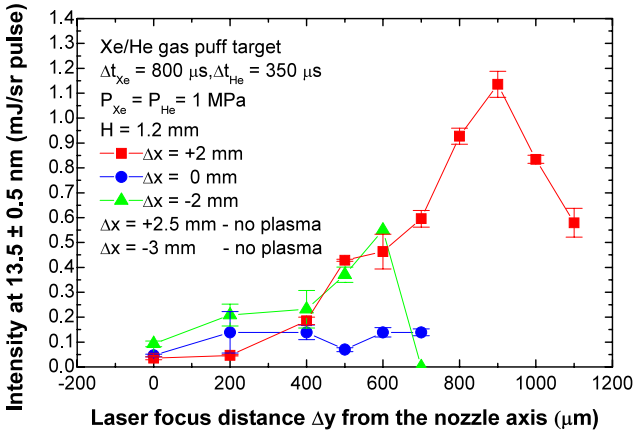

Fig. 19 Dependence of the EUV emission at 13.5 nm on the distance, Δy, between the laser focus and the nozzle axis for selected values of Δx

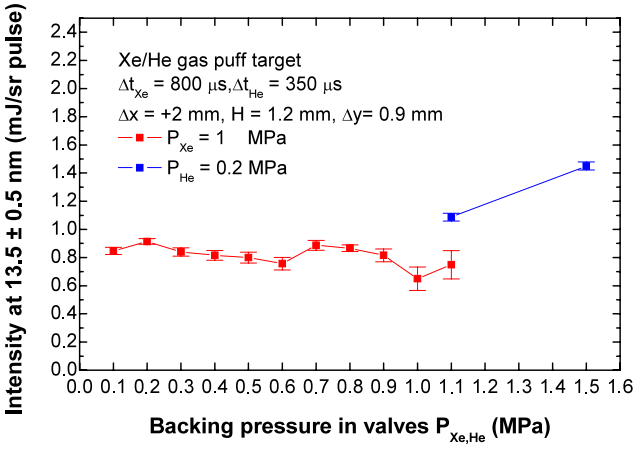

Fig. 21 Dependence of EUV emission at 13.5 nm on the backing pressure in the valves (the residual parameters are kept at their optimal values)

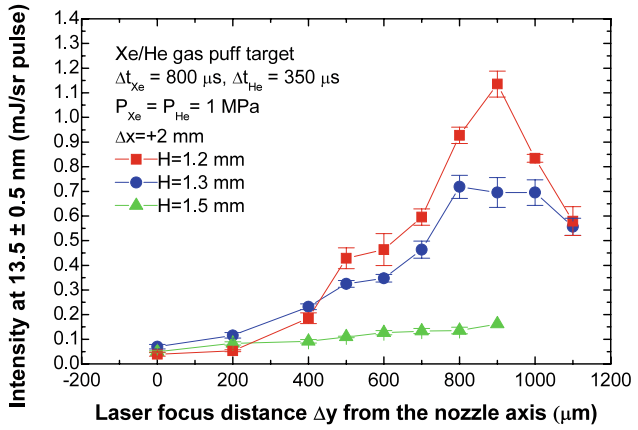

Fig. 20 Dependence of EUV emission at 13.5 nm on the distance Δy between the laser focus and the nozzle axis for selected values of H

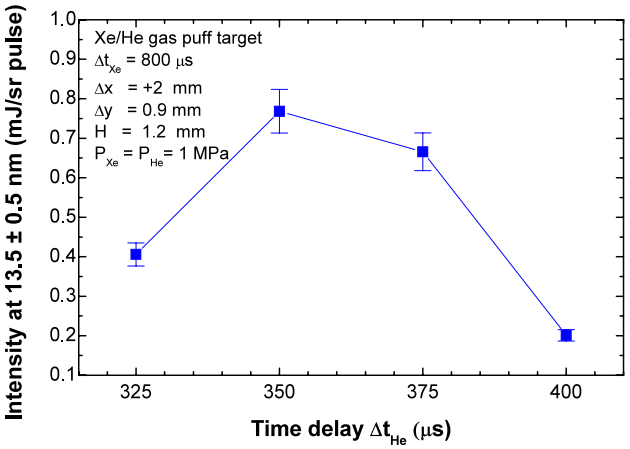

Fig. 22 Dependence of EUV emission at 13.5 nm on the time delay Δt_{He} (the residual parameters are kept at their optimal values)

6 Angular distribution of EUV radiation

Mostly, the EUV signal is recorded at a specific angle and, assuming spherical symmetry, is then averaged over a hemisphere. To estimate a correction factor for the EUV emission within 2π sr, angular emission measurements were performed. A detection-head with the AXUV-100Si/Zr detector and Mo/Si mirror coupled together was attached to a centering ring of the gasket. The angular position of the head was changed during the measurements and set at a specific angle. The diagram in Fig. 24 presents the angular EUV emission at 13.5 nm in the horizontal plane in the setup with the $f = 50$ mm lens.

For the optimum laser spot position in the gas puff target ($H = 1.2$ mm, $\Delta x = +2$ mm, $\Delta y = -900$ μm), the source evidently emits efficiently in the bottom half-plane only due to the opacity effect. Relatively low EUV emission was measured at angles $>60°$ in the transmitted laser beam direction. The support for this behavior comes from the focusing conditions (see inset).

7 EUV radiation intensity improvement by using differential pumping for the repetition rate regime

Self-absorption of the EUV radiation in Xe (opacity effect) for typical pressure conditions in the chamber (a few mbar during 10 Hz-operation) is not negligible. To minimize the self-absorption for the repetition-rate regime of the source, differential pumping was employed. The source chamber was sealed from the chamber containing the Mo/Si mirror (installed inside) and the photodiode detector using a diaphragm with a 1 mm diameter pinhole. Both chambers were evacuated separately.

The source chamber evacuated using a TriScroll PTS 300 pump (Varian prod.) and the chamber equipped with

the Mo/Si mirror by a turbo-drug pump (Pfeiffer prod.). In Fig. 25, the mean intensity at 13.5 nm for single-shot and repetition-rate operation, with and without the differential pumping, is presented. Without differential pumping, the intensity at 2-Hz repetition rate is only 10% of the maximum single-shot value. But using differential pumping at the maximally attainable 10-Hz repetition rate for the pumping laser, the intensity drops to half the value of the single-shot signal only. The amplitude analysis and the histogram of the EUV pulses are illustrated in Fig. 26.

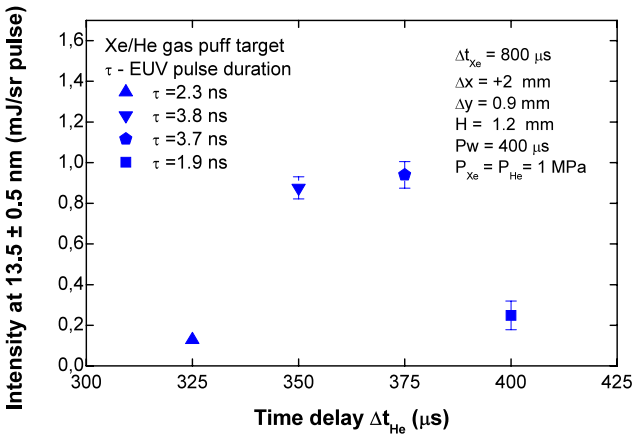

Fig. 23 Dependence of EUV emission at 13.5 nm on the time delay Δt_{He} (the residual parameters are kept at their optimal values)

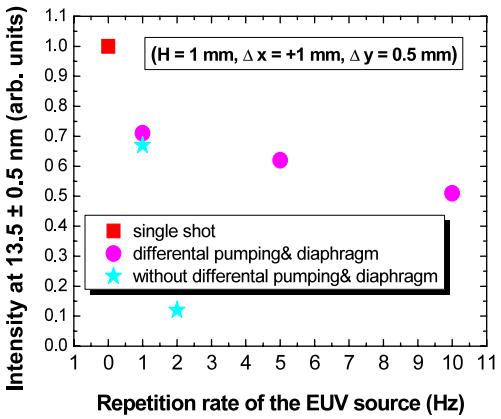

Fig. 25 EUV intensity at 13.5 nm depending on the repetition rate

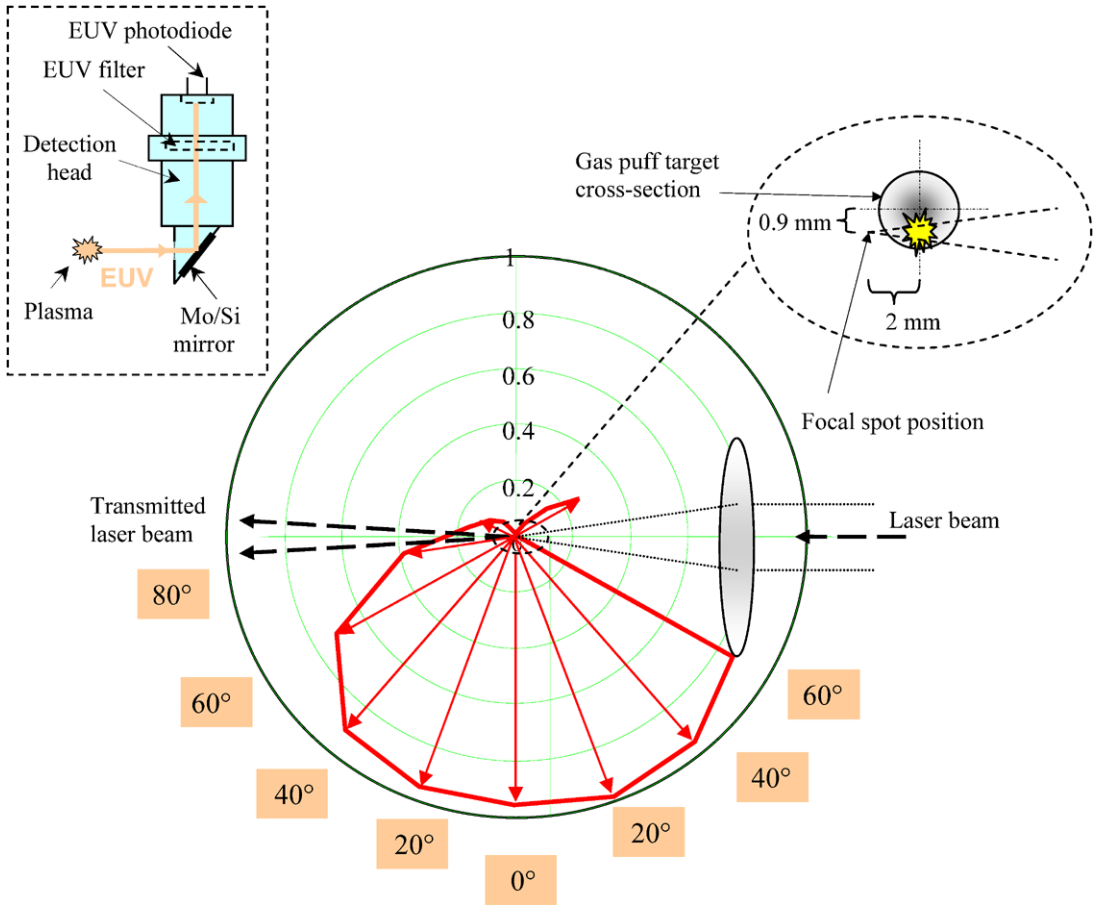

Fig. 24 Angular distribution of the EUV in-band emission in the horizontal plane. The *upper-right inset* shows the plasma location. The *upper-left inset* presents the detection-head scheme

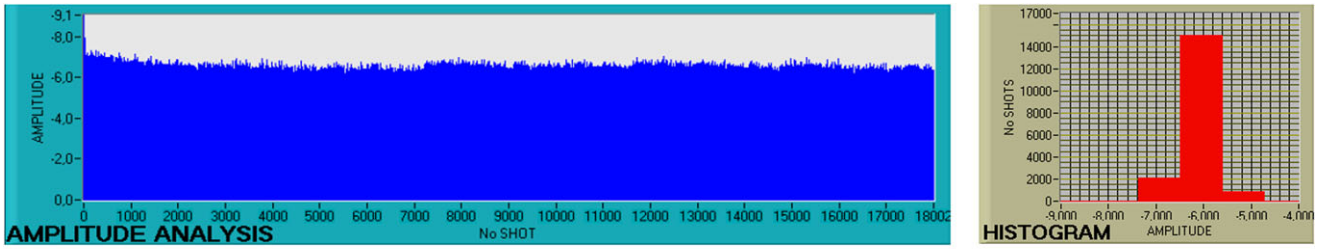

a b

Fig. 26 Results of the repetition rate measurements of the EUV source using LabVIEW environment. (**a**) amplitude analysis, (**b**) histogram

8 Thermodynamic plasma parameters

The plasma electron density N_e and the temperature T_e are estimated using the FLY suite code [48]. This code considers mainly collisional ionization and radiative- and three-body recombination. The basic thermodynamic parameters are the electron temperature and the electron density. They are deduced by comparison between the ratios of specific spectral lines of lithium-like oxygen ions taken from an experimental spectrum and the simulated spectra obtained from the FLY. The oxygen plasma is obtained after helium had been replaced by oxygen in the Xe/He gas puff target. The experimental data for comparison with artificial spectra are chosen for those parameters for which the xenon feature in the mixed Xe/O_2 plasma spectrum is comparable with the optimum spectrum of xenon observed for the Xe/He plasma spectrum for the maximum EUV in-band emission. The optimum electron density of 5×10^{20} cm^{-3} and temperature of 40 eV for the EUV emission is determined using this method that compares well with the calculated data found in the literature [38, 43]. To our knowledge, the plasma thermodynamic parameters were estimated for the first time using such a method.

Using an X-ray backlighting method, the atomic density of the target gas of about 10^{19}/cm^3 was calculated for the optimum EUV emission parameters. The electron density corresponding to the optimum atomic gas density in the gas puff target is about 10^{20} cm^{-3}, assuming a value of 10 for the average ionic charge Z^* (ionization stage), because the mentioned Xe^{10+} is the most abundant ion radiating at 13.5 nm. The optimum theoretical electron temperature of 32 eV for efficient EUV in-band emission from the xenon laser-produced plasma is reported in [43].

9 Comparison of experimental data of Xe laser-produced plasma radiation with modeling

The theoretical study of EUV emission of xenon and the conversion efficiency is done in three steps. First, all pertinent configurations are selected, then their energies and radiative transition rates are calculated using the HULLAC atomic suite of codes [49]. Opacity and emissivity files are subsequently determined using a simple collisional radiative model to compute the populations and the spectra employing the SCRIC code [50]. Finally, a simple hydroradiative model has been developed to evaluate the conversion efficiency of laser produced xenon plasmas in the EUV range.

The configurations are selected on an energy basis [42]. For Xe^{10+} whose maximum concentration is obtained around $T_e = 30$ eV [43, 51, 52], all configurations with energy below 300 eV ($= 10 \times T_e$) are kept. Above this energy, the configurations are supposed to be very little populated at moderate densities. Equivalent configurations are used for the other ions: $4p^64d^N$ is the ground configuration of ion $Xe^{(18-N)+}$, the singly excited configurations $4p^54d^{N+1}$ and $(4p^64d^{N-1})$4f, 5s, 5p, 5d, 5f, 5g, 6s, 6p, 6d, 6f, 6g, 6h, 7s, 7p, 7d, 7f, 8s, 8p, and the doubly excited configurations $4p^44d^{N+2}$; $(4p^54d^N)$4f, 5s, 5p, 5d, 5f, 6s, 6p; $(4p^64d^{N-2}4f)$4f, 5s, 5p, 5d, 6s, 6p; $(4p^64d^{N-2}5s)$5s, 5p, 5d, 5f, 5g, 6s, 6p, 6d, 6f, 7s, 7p; $(4p^64d^{N-2}5p)$5p, 5d, 6s, 6p; $4p^64d^{N-2}5d^2$ and $(4p^64d^{N-2}6s)$5f, 6p. The maximum principal quantum number $n = 8$ chosen for the singly excited configurations corresponds to the last existing layer in the ionic sphere model for averaged $Z^* = 10$ at $N_e = 10^{21}$ cm^{-3}.

The limit of 10 times the temperature makes it possible to have an accurate description of the remaining configurations for atomic densities below 10^{20} cm^{-3}. This is coherent with the experimental conditions for optimum EUV generation described before.

These configurations lead to a tremendous number of satellite lines, which strongly enhance the emissivity of EUV plasmas. The interaction of configurations sharpens the 4d-(4f/4p) group of resonant lines. It has been shown that the interaction of configurations has a strong influence on satellite lines and reduces the width of the main 4d-4f/4p-4d broad satellite structure [42, 51, 53]. Therefore, interaction of all configurations has systematically been included in our HULLAC calculations leading to energy matrices including more than 3000 levels.

The populations are calculated using collisional radiative (CR) equations including collisional ionization, radiative recombination, and three-body recombination rates as given in

the study of Colombant and Tonon [54]. Since the levels are not supposed to be in local thermodynamic equilibrium inside one ion, we used a similar model for level populations developed by S. B. Hansen et al. [55]. It includes collisional excitation and deexcitation and radiative decay as well.

For the radiative calculations, we use the code SCRIC to evaluate detailed emissivities and opacities of xenon in a broad range of 61 temperatures and 21 atomic densities (1–140 eV, 10^{17}–10^{20} cm^{-3}). All the ions from Xe^{3+} to Xe^{22+} are considered to evaluate emissivities and opacities, totalizing 1389 configurations, 284425 detailed levels and a hundred million lines. The line shape is calculated considering both Doppler and natural broadening with the Voigt profile.

The emission at 13.5 nm is dominated by Xe^{10+} ion. But, as presented in [42], most of the emission comes from the satellite lines of 4d–5p (doubly excited configurations decaying towards simply excited configurations with a 4d–5p scheme) when the density increases. The traditional resonant 4d–5p transition toward the ground state is less important above 10^{18} ion/cm^3 and of the same order of magnitude as the 6g–4f transition, which also contributes to the emission at 13.5 nm. Finally, the Xe^{9+} 4d–5p satellite lines also strongly enhance the emission at 13.5 nm and this explains why the maximum emission at 13.5 nm is reached for averaged ionization around 9.5+ and not above 10+. A very strong emission occurs around 11 nm, which reaches the Planckian limit even for a small plasma thickness. For this reason, opacity effects play an important role and require adaptation of the plasma length in order to control the radiative energy fluxes.

An autosimilar hydroradiative model has been created accounting for opacity effects, time dependence with full laser absorption, radiative losses, and hydrodynamic expansion as well. We assume a homogeneous spherical plasma. The spherical shape seems to be an reasonable approximation for the case of laser–gas puff interaction at optimum conditions as can be seen in Fig. 12c (in this case the shape is more ellipsoidal). As the mass and electron density is constant in the sphere (not in time but in space), we show that the speed inside the sphere remains homothetic and consequently all the formulas for the kinetic energy, radiative losses [53] of energy, and impulsion balance [56] remain very simple.

Figures 27–29 present the calculated radiative conversion efficiencies in the EUV range for the 3.9 ns, 0.5 J laser used in the experiment, for a broad range of initial ionic densities and initial plasma radii. In Fig. 27, the maximum conversion efficiency at 13.5 nm within 7.4% bandwidth reaches 3.4% at the initial radius of 240 μm and at the initial ionic density of 1.3×10^{19} cm^{-3}. This high conversion efficiency covers a large area: Radius from 110 to 410 μm and ionic density from 10^{20} to 3.2×10^{18} cm^{-3}. The calculated conversion efficiency for 2% bandwidth, presented in Fig. 28, shows the same features with the maximum value of 1.01%.

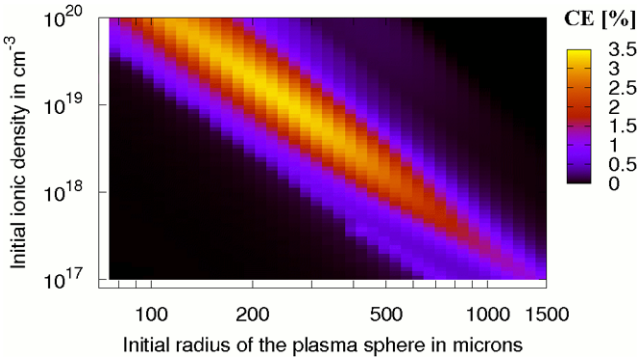

Fig. 27 Theoretical conversion efficiency within 7.4% bandwidth around 13.5 nm

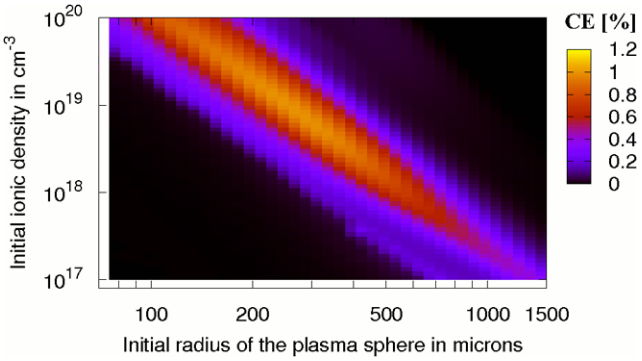

Fig. 28 Theoretical conversion efficiency within 2% bandwidth around 13.5 nm

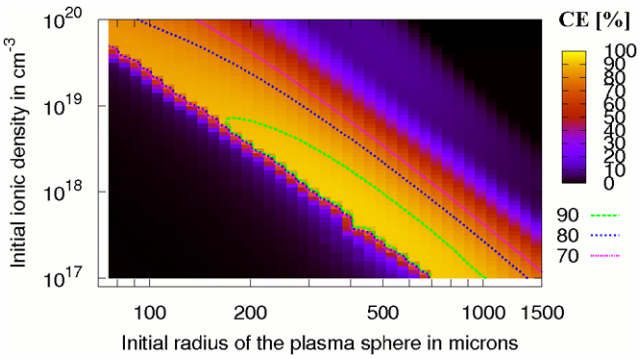

Fig. 29 Theoretical total radiation conversion efficiency (over the whole spectrum)

The ratio between both conversion efficiencies for 2% BW and 7.4% BW is nearly constant over the whole range of significant emission at 13.5 nm: 0.30 ± 0.02 to be compared with $0.42\%/2\% = 0.21$ ratio found with the semiconductor detectors (Sect. 5). In both graphs when the densities are high and the radii are large (upper right corner), the number of ions is very high in the plasma sphere and the overall energy invested in each ion plus its electrons is too small to reach the 10+ ionization, necessary for emission at 13.5 nm.

At the opposite corner (low densities, small radii the conversion efficiency is also very limited because the very few ions present absorb too much energy and reach immediately ionization stages that are too high. The total radiative conversion efficiency presented in Fig. 29 (the ratio of the radiative losses over the laser energy) shows very high rates all over the domain of high conversion efficiency at 13.5 nm (more than 75%). For this reason, it is not possible to make a pure hydro simulation without radiation losses as noticed in [56]. It shows also that it is possible to build a very efficient broadband radiation converter (mostly in the 10–14 nm region). The dramatic reduction of emission on the lower left corner is not relevant and comes from the lack of T_e data at 140 eV in our calculation.

The maximum conversion efficiency into 7.4% bandwidth is ∼3.4% at an initial radius of 240 μm and an initial ionic density of 1.3×10^{19} cm^{-3}. In comparison, the best experimental conversion efficiency is of 2% into 7.4% bandwidth as mentioned in Sect. 5. The experimental ionic density measured with a backlighter is $\sim 10^{19}$ cm^{-3} as mentioned in the previous section and the radius for the interacting zone is about 300 μm as can be seen in Fig. 12 (however, it can be can assumed that the radius of interaction zone is slightly smaller because the pinhole images show the emission which occurs during the expansion of the heated plasma). The discrepancy in the conversion efficiencies is higher for Xe/He experiments than for Xe/H experiments. In Figs. 2 and 3, the emission at 13.5 nm is 30% higher for hydrogen compared to helium. So, we may assume that the conversion efficiency into 7.4% bandwidth is 2.6% with hydrogen, which leads to a 23% overestimation in the theoretical model. This last discrepancy can be explained by the hypothesis of full laser absorption while 90% absorption is already very good in experimental conditions. A few percent may also be attributed to reabsorption by buffering hydrogen. Finally, the collisional radiative model assumes a very simple distribution of the population of levels only based on their energies, which may overestimate some of these populations.

Figure 30 shows the emission spectrum integrated over time and space for the best conversion efficiency. It is convoluted with a 0.2 eV and 1 eV broadening in order to compare with experimental spectra. It compares well with the Xe/He experimental spectrum in Fig. 4 between 12 and 14 nm. However, the main peak at 11 nm is more contrasted in the experiment. But, as noticed above, the comparison with Fig. 2 shows a better agreement with the Xe/H experimental spectrum when the 1 eV broadening is taken into account.

For this simulation, the maximum electron temperature reaches 34.6 eV and averaged Z^* reaches 10.3 (for $Z^* > 8.5$, Xe^{9+} and Xe^{10+} emit at 13.5 nm). At that moment the radius is 258 μm, but the emission at 13.5 nm lasts until the radius increases to 302 μm. The ionic density is 9.84×10^{18} cm^{-3}, while the electronic density is 1.01×10^{20} cm^{-3}. The emission at 13.5 nm lasts 4.4 ns. This is to be compared with the 3.7 to 3.8 ns of the experimental duration mentioned in Sect. 5.

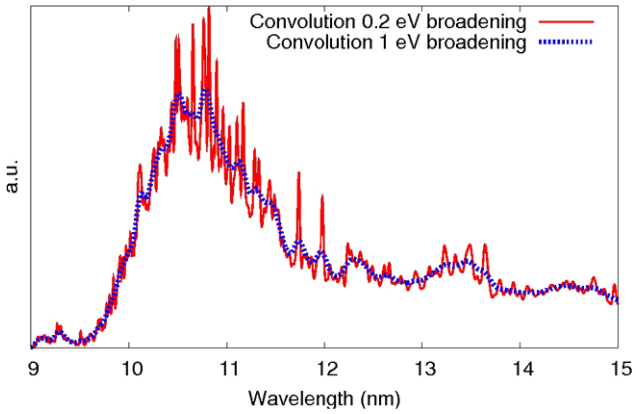

Fig. 30 Theoretical spectrum of Xe for the interaction of the laser pulse (3.9 ns, 0.5 J) and the gas puff (238 μm initial radius, 1.26×10^{19} cm^{-3} initial ionic density) with a convolution of 0.2 eV (*red solid line*) and 1 eV (*blue dotted line*) broadening

10 Conclusion

This paper investigates the laser-produced EUV source based on the Xe/He gas puff target. The distinctive advantage of this source, among others based on plasma, is its cleanliness. The source shows a few orders of magnitude greater intensity at 13.5 nm if compared to an X-ray tube and is of table-top size in contrary to, e.g., synchrotron facilities. The conversion efficiency of in-band intensity reaches 0.42%. It is shown that differential pumping makes possible a stable operation of the source with the maximum attainable laser repetition rate of 10 Hz. Using an original method, the plasma electron density and temperature are estimated to be in good agreement with theoretical calculations. The calculated spectra are in fair agreement with the experimental ones. This source can be useful for EUV metrology of multi-layer mirrors, masks, and resists.

Acknowledgements The research was performed under the European MEDEA+ programme and was funded by the State Committee for Scientific Research of Poland (KBN) under the Project SPUB-M Nr 217/E-284.

References

1. J. Jonkers, Plasma Sources Sci. Technol. **15**, S8 (2006)
2. S. Wurm, *EUVL manufacturing insertion*, Solid State Technology Online **23**, October (2006)
3. V. Banine, R. Moors, J. Phys. D, Appl. Phys. **37**, 3207 (2004)
4. U. Stamm, J. Phys. D, Appl. Phys. **37**, 3244 (2004)
5. K. Wakana, T. Abe, Y. Watanabe, T. Ishihara, T. Hori, T. Ohta, A. Kurosu, H. Komori, H. Nakarai, K. Kakizaki, A. Sumitani, J. Fujimoto, H. Mizoguchi, *Future of high power EUV sources* (presentation at http://www.euvlitho.com/2010/ABSTRACTS%202010%20EUVL%20Workshop.pdf)
6. L. Rymell, H.M. Hertz, Opt. Commun. **103**, 105 (1993)
7. H. Fiedorowicz, A. Bartnik, Z. Patron, P. Parys, Laser Part. Beams **12**(3), 471 (1994)
8. S. Ter-Avetisyan, U. Vogt, H. Stiel, M. Schnürer, I. Will, P.V. Nickles, J. Appl. Phys. **94**(9), 5489 (2003)
9. M. Segers, M. Bougeard, E. Caprin, T. Ceccotti, D. Normand, M. Schmidt, O. Sublemontier, Microelectr. Eng. **61–62**, 139 (2002)
10. G. Schriever, K. Bergmann, R. Lebert, J. Vac. Sci. Technol. B **17**(5), 2058 (1999)
11. B.A.M. Hansson, H.M. Hertz, J. Phys. D, Appl. Phys. **37**, 3233 (2004)
12. L.A. Shmaenok, C.C. De Bruijn, H.F. Fledderus, R. Stuik, A.A. Schmidt, D.M. Simanovski, A.V. Sorokin, T.A. Andreeva, F. Bijkerk, Proc. SPIE **3331**, 90 (1998)
13. K. Takenoshita, C.-S. Koay, M.C. Richardson, I.C.E. Turcu, Proc. SPIE **5037**, 792 (2003)
14. T. Mochizuki, C. Yamanaka, Proc. SPIE **733**, 23 (1987)
15. H. Fiedorowicz, A. Bartnik, R. Jarocki, J. Kostecki, J. Krzywiński, J. Mikołajczyk, R. Rakowski, A. Szczurek, M. Szczurek, J. Alloys Compd. **401**, 99 (2005)
16. H. Fiedorowicz, A. Bartnik, H. Daido, I.W. Choi, M. Suzuki, S. Yamagami, Opt. Commun. **184**, 161 (2000)
17. H. Fiedorowicz, A. Bartnik, Z. Patron, P. Parys, Appl. Phys. Lett. **62**(2), 2778 (1993)
18. H. Fiedorowicz, A. Bartnik, R. Jarocki, R. Rakowski, M. Szczurek, Appl. Phys. B **70**, 305 (2000)
19. H. Fiedorowicz, A. Bartnik, H. Daido, R. Jarocki, R. Rakowski, M. Suzuki, M. Szczurek, S. Yamagami, Proc. SPIE **4343**, 193 (2001)
20. D. Attwood, *Soft X-Rays and Extreme Ultraviolet Radiation: principles and applications* (Cambridge University Press, Cambridge, 2000)
21. T.W. Barbee, S. Mrowka, M.C. Hettrick, Appl. Opt. **24**, 883 (1985)
22. R. Stuik, E. Louis, A.E. Yakshin, P.C. Görts, E.L.G. Maas, F. Bijkerk, D. Schmitz, F. Scholze, G. Ulm, M. Haidl, J. Vac. Sci. Technol. B **17**(6), 2998 (1999)
23. T. Feigl, S. Yulin, N. Benoit, N. Kaiser, Microelectr. Eng. **83**, 703 (2006)
24. G. Schriever, K. Bergmann, R. Lebert, J. Appl. Phys. **83**(9), 4566 (1998)
25. N. Benoit, S. Yulin, T. Feigl, N. Kaiser, Physica B **357**, 222 (2005)
26. S. Yulin, N. Benoit, T. Feigl, N. Kaiser, Microelectr. Eng. **83**, 692 (2006)
27. R. Rakowski, A. Bartnik, H. Fiedorowicz, R. Jarocki, J. Kostecki, J. Krzywiński, J. Mikołajczyk, L. Pína, L. Ryć, M. Szczurek, H. Tichá, P. Wachulak, Opt. Appl. **XXXVI**(4), 593 (2006)
28. A. Bartnik, H. Fiedorowicz, R. Jarocki, L. Juha, J. Kostecki, R. Rakowski, M. Szczurek, Microelectr. Eng. **78–79**, 452 (2005)
29. A. Bartnik, H. Fiedorowicz, R. Jarocki, L. Juha, J. Kostecki, R. Rakowski, M. Szczurek, Appl. Phys. B **82**(4), 529 (2006)
30. A. Egbert, B. Mader, B. Tkachenko, A. Ostendorf, C. Fallnich, B.N. Chichkov, T. Mißalla, M.C. Schürmann, K. Gäbel, G. Schriever, U. Stamm, Microlith. Microfab. Microsyst. **2**, 136 (2003)
31. R. Klein, C. Laubis, R. Müller, F. Scholze, G. Ulm, Microelectr. Eng. **83**, 707 (2006)
32. R. Rakowski, A. Bartnik, H. Fiedorowicz, R. Jarocki, J. Kostecki, J. Krzywiński, J. Mikołajczyk, L. Ryć, M. Szczurek, P. Wachulak, Proc. SPIE **5958**, 706 (2005)
33. N. Nakano, H. Kuroda, T. Kita, T. Harada, Appl. Opt. **23**(14), 2386 (1984)
34. K. Eidmann, M. Kühne, P. Müller, G.D. Tsakiris, J. X-Ray Sci. Technol. **2**, 259 (1990)
35. S.S. Churilov, Y.N. Joshi, J. Reader, R.R. Kildiyarova, Phys. Scr. **70**, 126 (2004)
36. J. Bauche, C. Bauche-Arnoult, M. Klapisch, Phys. Scr. **37**, 659 (1988)
37. L. McKinney, *Xenon based laser plasma sources for photolithography*. Master thesis. University College Dublin, Dublin (2004)
38. G. O'Sullivan, A. Cummings, P. Dunne, P. Hayden, L. McKinney, N. Murphy, J. White, in *EUV Sources for Lithography*, ed. by V. Bakshi (SPIE, Bellingham, 2006)
39. G. O'Sullivan, A. Cummings, P. Dunne, K. Fahy, P. Hayden, L. McKinney, N. Murphy, E. Sokell, J. White, AIP Conf. Proc. **771**, 108 (2005)
40. M. Lysaght, D. Kilbane, N. Murphy, A. Cummings, P. Dunne, G. O'Sullivan, Phys. Rev. A **72**, 014502 (2005)
41. S.S. Churilov, Y.N. Joshi, J. Reader, Opt. Lett. **28**(16), 1478 (2003)
42. F. de Gaufridy de Dortan, J. Phys. B, At. Mol. Opt. Phys. **40**, 599 (2007)
43. N. Böwering, M. Martins, W.N. Partlo, I.V. Fomenkov, J. Appl. Phys. **95**(1), 16 (2004)
44. S. Chandrasekhar, *Hydrodynamic and Hydromagnetic Stability* (Clarendon, Oxford, 1961)
45. R.P.J. Town, A.R. Bell, Phys. Rev. Lett. **67**, 1863 (1991)
46. R. Doron, E. Behar, P. Mandelbaum, J.L. Schwob, H. Fiedorowicz, A. Bartnik, R. Jarocki, M. Szczurek, T. Wilhein, Phys. Rev. A **59**, 188 (1999)
47. J.F. Wyart, C. Bauche-Arnoult, E. Luc-Koenig, Phys. Scr. **32**, 103 (1985)
48. R.W. Lee, B.L. Whitten, R.E. Stout, J. Quant. Spectrosc. Radiat. Transf. **32**, 91 (1984)
49. A. Bar-Shalom, M. Klapisch, J. Oreg, J. Quant. Spectrosc. Radiat. Transf. **71**, 169 (2001)
50. F. de Gaufridy de Dortan, *SCRIC, un code pour calculer l'absorption et l'emission detaillees de plasmas hors equilibre inhomogenes et etendus*. CEA report No. 6115, CEA 2006
51. F. Gilleron, M. Poirier, T. Blenski, M. Schmidt, T. Ceccotti, J. Appl. Phys. **94**, 2086 (2003)
52. M. Poirier, T. Blenski, F. de Gaufridy de Dortan, F. Gilleron, J. Quant. Spectrosc. Radiat. Transf. **99**, 482 (2006)
53. A. Sasaki, K. Nishihara, M. Murakami, F. Koike, T. Kagawa, T. Nishikawa, K. Fujima, T. Kawamura, H. Furukawa, Appl. Phys. Lett. **85**, 5857 (2004)
54. D. Colombant, G.F. Tonon, J. Appl. Phys. **44**, 3524 (1973)
55. S.B. Hansen, K.B. Fournier, C. Bauche-Arnoult, J. Bauche, O. Peyrusse, J. Quant. Spectrosc. Radiat. Transf. **99**, 272 (2006)
56. T. Auguste, F. de Gaufridy de Dortan, T. Ceccotti, J.F. Hergott, O. Sublemontier, D. Descamps, M. Schmidt, J. Appl. Phys. **101**, 043302.1-13 (2007)